Open foundry platform for high-performance electronic-photonic integration

Jason S. Orcutt,[1,*] Benjamin Moss,[1] Chen Sun,[1] Jonathan Leu,[1] Michael Georgas,[1] Jeffrey Shainline,[2] Eugen Zgraggen,[1] Hanqing Li,[1] Jie Sun,[1] Matthew Weaver,[1] Stevan Urošević,[1,2] Miloš Popović,[2] Rajeev J. Ram[1] and Vladimir Stojanović[1]

[1] *Department of Electrical Engineering and Computer Science, Massachusetts Institute of Technology, 77 Massachusetts Ave, Cambridge, Massachusetts 02139, USA*

[2] *Department of Electrical, Computer and Energy Engineering, University of Colorado at Boulder, Boulder, Colorado 80309, USA*

[*] *jsorcutt@mit.edu*

Abstract: This paper presents photonic devices with 3 dB/cm waveguide loss fabricated in an existing commercial electronic 45 nm SOI-CMOS foundry process. By utilizing existing front-end fabrication processes the photonic devices are monolithically integrated with electronics in the same physical device layer as transistors achieving 4 ps logic stage delay, without degradation in transistor performance. We demonstrate an 8-channel optical microring-resonator filter bank and optical modulators, both controlled by integrated digital circuits. By developing a device design methodology that requires zero process infrastructure changes, a widely available platform for high-performance photonic-electronic integrated circuits is enabled.

©2012 Optical Society of America

OCIS codes: (250.3140) Integrated optoelectronic circuits; (250.7360) Waveguide modulators; (250.5300) Photonic integrated circuits.

References and links

1. M. Hochberg and T. Baehr-Jones, "Towards fabless silicon photonics," Nat. Photonics **4**(8), 492–494 (2010).
2. P. Dumon, W. Bogaerts, R. Baets, J. M. Fedeli, and L. Fulbert, "Towards foundry approach for silicon photonics: silicon photonics platform ePIXfab," Electron. Lett. **45**, 13–14 (2009).
3. M. Hochberg, "Fabless nanophotonics," in *Conference on Lasers and Electro-Optics* (Optical Society of America, 2011), CWM1.
4. C. Gunn, "CMOS photonics for high-speed interconnects," IEEE Micro **26**(2), 58–66 (2006).
5. L. C. Kimerling, D. Ahn, A. B. Apsel, M. Beals, D. Carothers, Y. K. Chen, T. Conway, D. M. Gill, M. Grove, C. Y. Hong, M. Lipson, J. Liu, J. Michel, D. Pan, S. S. Patel, A. T. Pomerene, M. Rasras, D. K. Sparacin, K. Y. Tu, A. E. White, and C. W. Wong, "Electronic-photonic integrated circuits on the CMOS platform," Proc. SPIE **6125**, 6–15 (2006).
6. Y. Vlasov, W. M. J. Green, and F. Xia, "High-throughput silicon nanophotonic wavelength-insensitive switch for on-chip optical networks," Nat. Photonics **2**(4), 242–246 (2008).
7. I. A. Young, E. Mohammed, J. T. S. Liao, A. M. Kern, S. Palermo, B. A. Block, M. R. Reshotko, and P. L. D. Chang, "Optical I/O technology for tera-scale computing," IEEE J. Solid-St. Circulation **45**, 235–248 (2010).
8. W. A. Zortman, D. C. Trotter, A. L. Lentine, G. Robertson, and M. R. Watts, "Monolithic integration of silicon electronics and photonics," in *Winter Topicals (IEEE* 2011), 139–140.
9. J. S. Orcutt, A. Khilo, C. W. Holzwarth, M. A. Popović, H. Li, J. Sun, T. Bonifield, R. Hollingsworth, F. X. Kärtner, H. I. Smith, V. Stojanović, and R. J. Ram, "Nanophotonic integration in state-of-the-art CMOS foundries," Opt. Express **19**(3), 2335–2346 (2011).
10. S. Narasimha, K. Onishi, H. M. Nayfeh, A. Waite, M. Weybright, J. Johnson, C. Fonseca, D. Corliss, C. Robinson, M. Crouse, D. Yang, C. H. J. Wu, A. Gabor, T. Adam, I. Ahsan, M. Belyansky, L. Black, S. Butt, J. Cheng, A. Chou, G. Costrini, C. Dimitrakopoulos, A. Domenicucci, P. Fisher, A. Frye, S. Gates, S. Greco, S. Grunow, M. Hargrove, J. Holt, S. J. Jeng, M. Kelling, B. Kim, W. Landers, G. Larosa, D. Lea, M. H. Lee, X. Liu, N. Lustig, A. McKnight, L. Nicholson, D. Nielsen, K. Nummy, V. Ontalus, C. Ouyang, X. Ouyang, C. Prindle, R. Pal, W. Rausch, D. Restaino, C. Sheraw, J. Sim, A. Simon, T. Standaert, C. Y. Sung, K. Tabakman, C. Tian, R. Van Den Nieuwenhuizen, H. Van Meer, A. Vayshenker, D. Wehella-Gamage, J. Werking, R. C. Wong, J. Yu, S. Wu, R. Augur, D. Brown, X. Chen, D. Edelstein, A. Grill, M. Khare, Y. Li, S. Luning, J. Norum, S. Sankaran, D. Schepis, R. Wachnik, R. Wise, C. Warm, T. Ivers, and P. Agnello, "High performance 45-nm SOI technology with enhanced strain, porous low-k BEOL, and immersion lithography," in *International Electron Devices Meeting* (IEEE, 2006), 1–4.

#163082 - $15.00 USD Received 15 Feb 2012; revised 29 Mar 2012; accepted 2 Apr 2012; published 15 May 2012

11. J. Youn, M. Lee, K. Park, and W. Choi, “A 10-Gb/s 850-nm CMOS OEIC Receiver with a Silicon Avalanche Photodetector,” IEEE J. Quantum Electron. **48**(2), 229–236 (2012).
12. B. Jang and A. Hassibi, “Biosensor systems in standard CMOS processes: fact or fiction?” IEEE Trans. Ind. Electron. **56**(4), 979–985 (2009).
13. Akustica, “Technology,” retrieved February 7, 2012, http://www.akustica.com/Technology.asp.
14. C.-L. Dai, F.-Y. Xiao, Y.-Z. Juang, and C.-F. Chiu, “An approach to fabricating microstructures that incorporate circuits using a post-CMOS process,” J. Micromech. Microeng. **15**(1), 98–103 (2005).
15. R. Kalla, B. Sinharoy, W. J. Starke, and M. Floyd, “Power7: IBM's next-generation server processor,” IEEE Micro **30**(2), 7–15 (2010).
16. L. Sungjae, B. Jagannathan, S. Narasimha, A. Chou, N. Zamdmer, J. Johnson, R. Williams, L. Wagner, K. Jonghae, J. O. Plouchart, J. Pekarik, S. Springer, and G. Freeman, “Record RF performance of 45-nm SOI CMOS Technology,” in *Electron Devices Meeting (IEEE* 2007), 255–258.
17. J. S. Orcutt and R. J. Ram, “Photonic device layout within the foundry CMOS design environment,” IEEE Photon. Technol. Lett. **22**(8), 544–546 (2010).
18. J. S. Orcutt, A. Khilo, M. A. Popovic, C. W. Holzwarth, B. Moss, L. Hanqing, M. S. Dahlem, T. D. Bonifield, F. X. Kartner, E. P. Ippen, J. L. Hoyt, R. J. Ram, and V. Stojanovic, “Demonstration of an electronic photonic integrated circuit in a commercial scaled bulk CMOS process,” in *Conference on Lasers and Electro-Optics* (Optical Society of America, 2008), CTuBB3.
19. J. S. Orcutt, “Scaled CMOS photonics,” in *Photonics in Switching* (Optical Society of America, 2010), PMC4.
20. S. Sridaran and S. A. Bhave, “Nanophotonic devices on thin buried oxide Silicon-On-Insulator substrates,” Opt. Express **18**(4), 3850–3857 (2010).
21. P. Dong, W. Qian, H. Liang, R. Shafiiha, N.-N. Feng, D. Feng, X. Zheng, A. V. Krishnamoorthy, and M. Asghari, “Low power and compact reconfigurable multiplexing devices based on silicon microring resonators,” Opt. Express **18**(10), 9852–9858 (2010).
22. F. N. Xia, L. Sekaric, and Y. Vlasov, “Ultracompact optical buffers on a silicon chip,” Nat. Photonics **1**(1), 65–71 (2007).
23. S. K. Selvaraja, P. Jaenen, W. Bogaerts, D. V. Thourhout, P. Dumon, and R. Baets, “Fabrication of photonic wire and crystal circuits in silicon-on-insulator using 193-nm optical lithography,” J. Lightwave Tech. **27**(18), 4076–4083 (2009).
24. M. A. Popovic, T. Barwicz, E. Ippen, and F. X. Kärtner, “Global design rules for silicon microphotonic waveguides: sensitivity, polarization and resonance tunability,” in *Conference on Lasers and Electro-Optics* (Optical Society of America, 2006), CTuCC1.
25. M. A. Popovic, *Theory and design of high-index-contrast microphotonic circuits* (Massachusetts Institute of Technology, 2008).
26. D. A. B. Miller, “Device requirements for optical interconnects to silicon chips,” Proc. IEEE **97**(7), 1166–1185 (2009).
27. M. Georgas, J. Leu, B. Moss, S. Chen, and V. Stojanovic, “Addressing link-level design tradeoffs for integrated photonic interconnects,” in *Custom Integrated Circuits Conference* (IEEE, 2011), 1–8.
28. P. Dong, W. Qian, H. Liang, R. Shafiiha, X. Wang, D. Feng, G. Li, J. E. Cunningham, A. V. Krishnamoorthy, and M. Asghari, “1x4 reconfigurable demultiplexing filter based on free-standing silicon racetrack resonators,” Opt. Express **18**(24), 24504–24509 (2010).
29. M. Georgas, J. Orcutt, R. J. Ram, and V. Stojanovic, “A monolithically-integrated optical receiver in standard 45-nm SOI,” in *European Solid State Circuits Conference* (IEEE, 2011), 407–410.
30. J. Leu and V. Stojanovic, “Injection-locked clock receiver for monolithic optical link in 45nm SOI,” in *Asian Solid State Circuits Conference* (IEEE, 2011), 149–152.
31. Q. Xu, B. Schmidt, S. Pradhan, and M. Lipson, “Micrometre-scale silicon electro-optic modulator,” Nature **435**(7040), 325–327 (2005).
32. Q. Xu, S. Manipatruni, B. Schmidt, J. Shakya, and M. Lipson, “12.5 Gbit/s carrier-injection-based silicon micro-ring silicon modulators,” Opt. Express **15**(2), 430–436 (2007).
33. F. Liu, D. Patil, J. Lexau, P. Amberg, M. Dayringer, J. Gainsley, H. F. Moghadam, Z. Xuezhe, J. E. Cunningham, A. V. Krishnamoorthy, E. Alon, and R. Ho, “10 Gbps, 530 fJ/b optical transceiver circuits in 40 nm CMOS,” in *Symposium on VLSI Circuits* (IEEE, 2011), 290–291.
34. M. R. Watts, W. A. Zortman, D. C. Trotter, R. W. Young, and A. L. Lentine, “Vertical junction silicon microdisk modulators and switches,” Opt. Express **19**(22), 21989–22003 (2011).

1. Introduction

Standardized fabrication of microchips with silicon photonic devices and circuits in multi-user fabrication facilities, known as foundries, promises to dramatically increase the pace of technology innovation in ways analogous to the late 20th-century transformation of the CMOS electronics industry [1]. Recently, photonics-only mask-shared fabrication runs have greatly increased access to advanced processing technology [2,-3]. Integration of photonics with electronic circuits, however, has not provided widespread technology access or achieved monolithic integration of high-performance electronic and photonic devices. Past advances

#163082 - $15.00 USD Received 15 Feb 2012; revised 29 Mar 2012; accepted 2 Apr 2012; published 15 May 2012
(C) 2012 OSA

using proprietary facilities have utilized older CMOS technology to enable process modification [4–8] or achieved limited photonics performance [9]. In this work, high performance electronic and photonic devices are monolithically integrated within a 45 nm transistor gate length silicon-on-insulator (SOI) CMOS foundry process [10]. By adapting photonic device design and layout to maintain compliance with existing foundry design rules, zero in-foundry process changes are required. As such, the existing manufacturing infrastructure of the electronics community can be directly leveraged to enable access to state-of-the-art technology at low cost. The 2.9 mm x 2.9 mm die presented here was fabricated in a multi-project run in which the ~850 mm^2 field size lithographic masks and all wafer-level

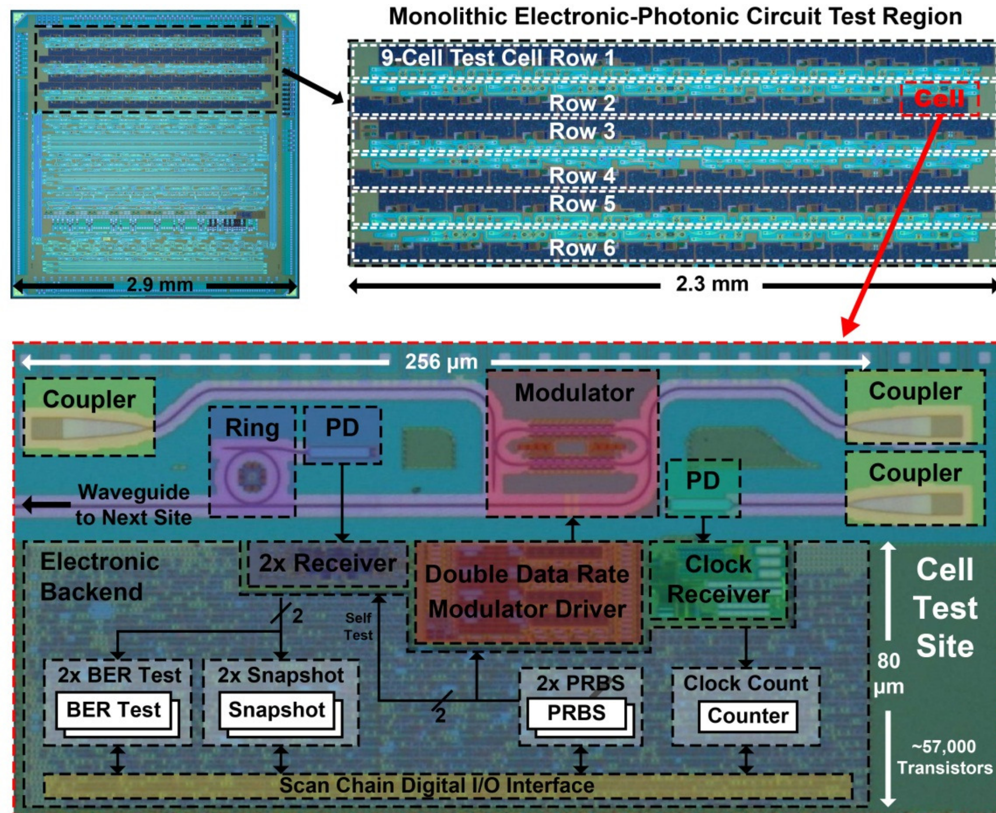

Fig. 1. Illustrated micrograph of the fabricated electronic-photonic integration test die containing 54 independently addressable electronic-photonic test cells. Each digitally interfaced cell contains the pseudorandom bit sequence (PRBS) generators, samplers and comparators necessary for in situ link signal monitoring and bit error rate (BER) testing. Only the transmit end of an electronic-photonic link is reported in this work.

processes of the advanced CMOS line were shared by many standard electronics customers. In past work, diverse application areas including optical communication receivers [11], bio-sensing [12] and micro-electrical mechanical systems (MEMS) [13, 14] have leveraged the existing electronics foundry manufacturing infrastructure to integrate non-standard devices. In this work, we present an electronics-photonics platform demonstration implemented as the array of 54 digitally interfaced test cells shown in Fig. 1.

2. CMOS foundry integration methodology

The photonic devices, including dense wavelength division multiplexing (DWDM) filters and electro-optic modulators, are patterned in the standard process using available design layers

#163082 - $15.00 USD Received 15 Feb 2012; revised 29 Mar 2012; accepted 2 Apr 2012; published 15 May 2012
(C) 2012 OSA

traditionally used for transistor fabrication. Photonic devices were fabricated in the standard processing flow of the IBM 12SOI 45 nm SOI-CMOS foundry alongside 3-million transistors. The design was submitted for mask aggregation at the Kansas City Plant (KCP) as part of a Trusted Access Program Office (TAPO) shuttle run. Physical process details, including the cross-sectional layer type and thickness information explicitly not reported in this work, are provided as part of the standard electronic design kit that is made available to IBM foundry customers under a non-disclosure agreement. A subset of process and performance information regarding this electronics process can be found in IBM publications [10,15,16].

Design preparation was performed in Cadence Virtuoso and Encounter tools to enable electronic-photonic integration and compliant design submission [17]. Local pattern density process compliance was maintained in mask design while excluding optically-lossy metals from a 2-3 µm region around the waveguides [17]. Custom auto-fill routines were developed to identify design coordinates requiring fill to meet pattern density targets using a script written for Mentor Graphics Calibre. High-density, 0.8 µm x 0.8 µm, metal fill cells were then automatically inserted at these design coordinates using scripts developed inside Cadence Virtuoso. Several waivers for violations of standard process design rules were obtained through the standard foundry infrastructure. Most resulted from photonic devices being erroneously flagged during the automated design rule check processing as improperly formed electronic devices. The smooth photonic shapes such as rings and bends were discretized onto the allowed mask address grid and represented in the submitted database as many rectangles [17]. Geometry waivers for the small, nanometer-scale notches formed by this discretization were also obtained, as these shapes have been shown to present no structural threat to process yield in several process generations from multiple manufacturers [9, 17–19].

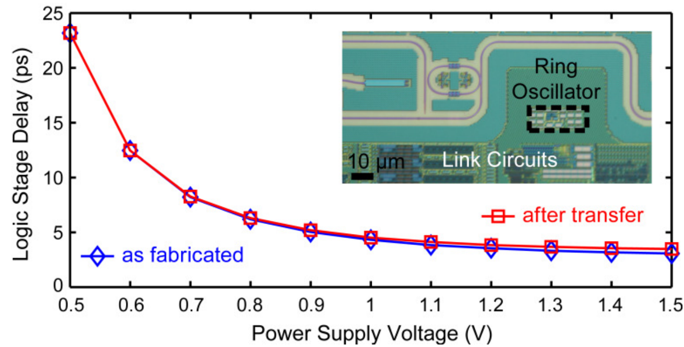

Fig. 2. Plot of measured logical stage delay for ring oscillators both before and after substrate transfer (described in Section 3) as a function of supply voltage. The nominal supply voltage for this process is 1V. The delay is extracted by dividing the measured oscillation frequency by the number of stages.

#163082 - $15.00 USD Received 15 Feb 2012; revised 29 Mar 2012; accepted 2 Apr 2012; published 15 May 2012
(C) 2012 OSA

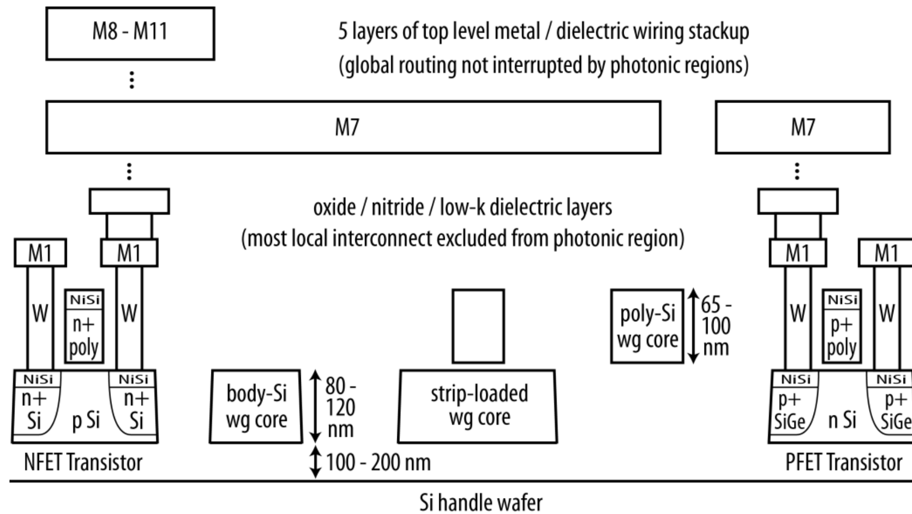

Fig. 3. Cross section cartoon of photonic integration within a scaled thin-SOI platform. The single-crystalline silicon waveguide core (body-Si) is formed in the layer that functions as the transistor body in the standard electronics process. The polysilicon (poly-Si) waveguide core is formed in the layer that functions as the transistor gate in the standard electronics process. The proximity of the two layers enables the formation of a strip-loaded waveguide as well.

Electronic ring oscillators, formed by an odd number of inverting logic stages and placed in close proximity of the photonic devices in the photonic integration regions, indicate no observable transistor performance degradation verifying that photonic devices can be integrated closely with high-performance transistors. The logic stage delay characterized by the oscillator resonant frequency is shown in Fig. 2. The achieved switching time of less than 5 ps is the fastest demonstration of logic transistor performance within a monolithically integrated photonic platform [16].

3. Substrate-transfer post-processing

Since the SOI-CMOS electronics process is optimized for transistor performance and low thermal impedance, the buried oxide (BOX) layer that separates the silicon layer from the handle wafer is thinner than 200 nm as shown in Fig. 3. This is in contrast to the 2-3 μm buried oxide thickness that is common for photonics SOI wafers. The as-fabricated wafers therefore do not provide sufficient low-index cladding thickness underneath the silicon waveguide core to eliminate substrate leakage loss. Post-processing that can locally remove the underlying silicon has been demonstrated previously for various photonics applications [9,20,21] as well as for commercial volume production of MEMS [13]. For faster characterization turnaround, in this work we instead use a substrate-transfer process. The die received from the foundry were mounted pad-side down to an oxidized silicon wafer with Crystalbond 509. The exposed silicon substrate of the die was then removed using 10 s etch, 50 s pump cycles of XeF_2 gas. Once the substrate is completely removed, a thermally and electrically conductive transfer substrate of 6H-SiC is bonded to the CMOS layer stack using Norland Optical Adhesive 71. This optically clear adhesive with a working temperature of 125 °C is UV cured in place and aged in a 50 °C oven for 12 h. Next, the transferred die is removed from the handle wafer by melting the Crystalbond on a 85 °C hot plate. After cleaning, the transferred die is wire bonded into a 208-pin ceramic pin-grid array package (Spectrum CPG20809). The received packaged samples were then used in the optoelectronic characterization experiments. After all post-processing is completed, we verify that the integrated transistor characteristics remain within 5% of their as-fabricated state at nominal supply voltage by re-measuring the ring oscillator after transfer as shown in Fig. 2. Similar

#163082 - $15.00 USD Received 15 Feb 2012; revised 29 Mar 2012; accepted 2 Apr 2012; published 15 May 2012
(C) 2012 OSA

experiments to verify that wafer-scale, front-side localized substrate removal post-processing does not impact transistor characteristics have been reported in the post-CMOS MEMS literature [14].

4. Waveguide loss characterization

To be an enabling technology for a broad range of photonics applications, the integrated waveguide loss must be comparable to the best available silicon photonics results using photolithography that are in the range of 2-3 dB/cm for strongly confined modes [22, 23]. In the SOI-CMOS process, the single-crystalline silicon layer that forms the transistor floating body may be patterned to form an oxide-clad rectangular waveguide as shown in Fig. 3. This is in contrast to the previous zero-change integration work in bulk-CMOS [9], where the polysilicon transistor gate was used. Although the silicon layer thickness of less than 100 nm and the specific surrounding dielectric environment is unique to the deeply-scaled electronics process used, the integrated waveguides otherwise closely resemble waveguides from past electronic integration work [4–8] and photonics-only processes [22, 23]. Previously proposed optimized silicon waveguide geometries in fact come close to this available ~100 nm thickness [24, 25]. Strongly-confined body silicon waveguide propagation loss is measured to be approximately 3 dB/cm from 1260 nm to 1350 nm as well as from 1560 nm to 1630 nm as shown in Fig. 4(a-b). The polysilicon layer present in the process as the transistor gate, however, has waveguide loss greater than 50 dB/cm for all wavelengths of interest in agreement with past bulk-CMOS results [9]. The polysilicon layer, available on top of the single-crystalline silicon layer, may still be leveraged to enable a broader range of device geometries. For example, polysilicon-on-silicon strip-loaded (rib) waveguides in which the polysilicon layer forms the ribs are used to form the optical modulators reported in this work.

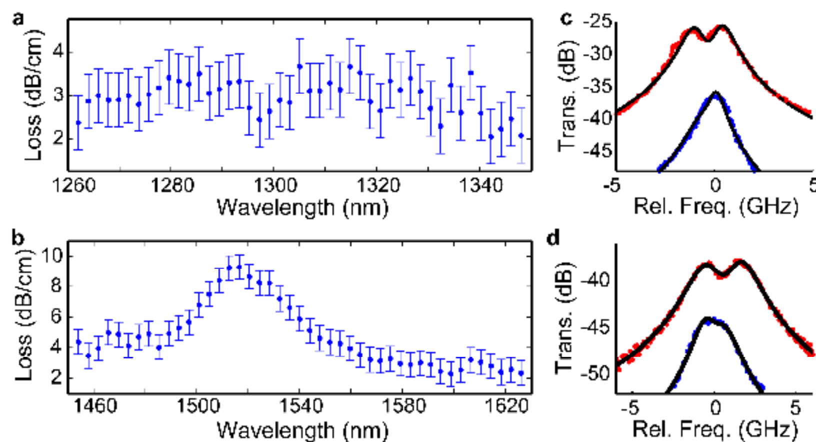

Fig. 4. The waveguide loss was measured in structures with 4.1 mm differential length, analogous to the cut-back method, on four samples. Propagation loss in 470 nm wide waveguides was measured from 1260 nm to 1350 nm (a) and in 700 nm wide waveguides was measured from 1450 nm to 1630 nm (b). Measured fiber-to-fiber transmission spectra of the drop ports of moderately-coupled (red data points) and weakly-coupled (blue data points) 20 µm radius rings at 1280 nm (c) and 1550 nm (d) are fit to coupled resonator models (solid black lines) for intrinsic quality factor extraction. The dip at the center of the resonance results from scattering-induced coupling between the forward and backward propagating ring modes. For the weakly-coupled rings, quality factors of 227,000 and 112,000 were extracted for 1280 nm and 1550 nm respectively. Ring and bus waveguide widths were 470 nm for 1280 nm and 670 nm for 1550 nm. Coupling gaps of 830 nm and 740 nm were used for 1550 nm; 660 nm and 600 nm were used for 1280 nm.

#163082 - $15.00 USD Received 15 Feb 2012; revised 29 Mar 2012; accepted 2 Apr 2012; published 15 May 2012
(C) 2012 OSA

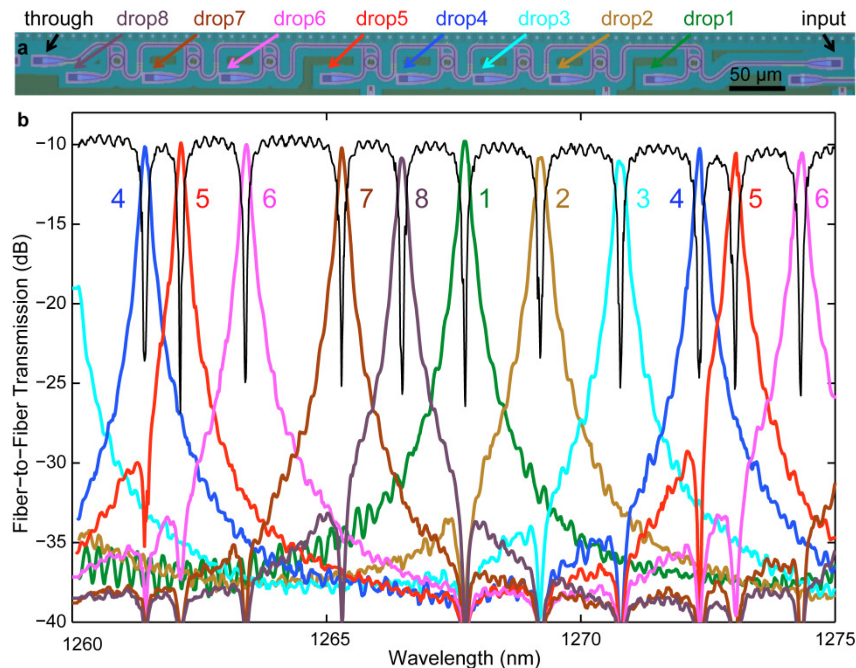

Fig. 5. (a) Optical micrograph of an 8-channel filter bank implemented with 7.0 μm nominal radius first-order ring-resonator filters. Design dimensions: 470 nm ring and bus waveguide widths, 217 nm input and drop side ring-bus coupling gaps. (b) Filter bank transfer function for all ports as measured for fiber-to-fiber transmission.

The low waveguide loss of the single crystalline silicon layer, comparable with the state-of-the-art for most wavelengths, enables the fabrication of highly-efficient resonant photonic devices. Extracted intrinsic quality factors of 227,000 and 112,000 were obtained for 1280 nm and 1550 nm rings respectively as shown in Fig. 4(c) and 4(d). The corresponding waveguide losses are calculated to be 3.7 dB/cm and 4.6 dB/cm by using group indices of 3.92 and 2.94 as calculated from the free spectral ranges for 1280 nm and 1550 nm light respectively. In addition to confirming the order of magnitude of the waveguide losses measured by the paperclips, the resonator quality factor measurements confirm that the curved waveguide mode present in the ring also exhibits low propagation loss.)

5. Wavelength division multiplexing filter banks

The high-resolution photolithography used in this 45 nm process enables the precise lateral dimension control that is critical to a wide variety of photonic devices [9, 22-23]. An important example of such a device is the ring resonator filter bank that enables the bandwidth-density advantage of silicon-photonics for interconnect applications by enabling dense wavelength division multiplexing (DWDM) [21, 26-27]. In the design of the filter banks presented, the target resonant frequency of each channel is not designed to a fixed absolute value due to the uncertainty in the fabricated silicon layer thickness and ambient temperature during operation. Instead, the eight channels are designed to be evenly distributed across the free spectral range (FSR) of a single filter. The fabrication precision allows the measured 8-channel filter bank, shown in Fig. 5(a), to be composed of evenly distributed channels by increasing the ring radius in steps of 12 nm. The as-fabricated filter transmission characteristics, shown in Fig. 5(b), verify channels distributed throughout the FSR in order, yielding no gaps or perturbations in the wavelength grid. The on-resonance filter drop loss is

#163082 - $15.00 USD Received 15 Feb 2012; revised 29 Mar 2012; accepted 2 Apr 2012; published 15 May 2012
(C) 2012 OSA

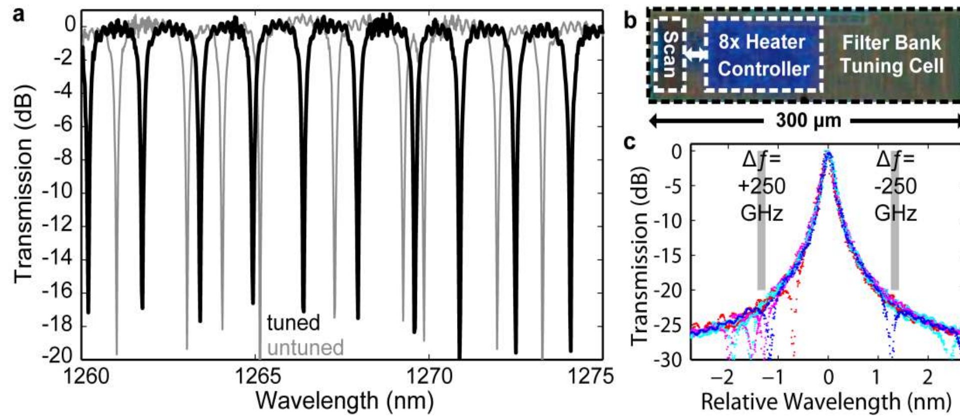

Fig. 6. The aggregate filter bank through port transmission function (a) is measured before and after the heater tuning by the integrated controller (b). Heater output parameters for each channel were programmed into the on-chip controller after measurement of the untuned transmission function. The overlaid drop port characteristics for all 8 channels are shown in (c) to demonstrate less than −20 dB cross talk between adjacent 250 GHz spaced channels across the full 30 GHz channel width for all ports.

measured to be less than 1 dB for all channels. The measured 10 dB fiber-to-fiber loss is dominated by expected theoretical loss of the simple vertical grating coupler designs used in this initial work.

The integrated electronics, shown in Fig. 6(b), were then used to thermally tune the 30 GHz full-width at half-maximum (FWHM) filters to a 250 GHz grid on the 2.04 THz FSR. Once tuned, the adjacent channel cross-talk is below −20 dB as shown by the overlaid drop ports in Fig. 6(c). While the filter tuning efficiency of 2.6 mW/nm is relatively low [28] due to the simple heater geometry and sample transfer process used in this work, the total power required to tune the filters to the grid was only 10.3 mW including the integrated open-loop controllers. In comparison to the best published full FSR tuning power of 2.9 mW for a single ring filter channel excluding external controller power [28], the lithographic precision reduces total thermal tuning power and enables further power optimization through nearest-channel locking aided by the transistor bit-reordering backend in proposed link architectures [27].

6. Integrated electro-optic transmitters

As shown in Fig. 1, each digital backend cell in the integration test platform includes a locally driven optical modulator and photodiodes connected to data [29] and clock receivers [30]. Due to a lack of *a priori* process knowledge, detectors primarily served as test structures for both material characterization and understanding circuit integration for this chip. Measurements of the epitaxial SiGe material, which is present in the process for transistor strain engineering [16] and is the intended absorber for detector designs, demonstrated 0.5 dB/μm excess absorption at 1240 nm when compared to similarly-sized, silicon-only waveguides, projecting ~20 μm linear detector length. First-generation detectors are ~1% efficient due to extrinsic losses and are not reported in detail in this work. The below 1300 nm operating wavelengths of the modulator and filter bank presented in this paper were chosen for eventual interaction with future generations of these silicon germanium detectors.

The resonant optical modulators driven by the integrated electronics were implemented using the strip-loaded (rib) waveguide geometry shown in Fig. 6(b). The lateral p-i-n diode that is used for carrier-plasma modulation in forward-bias was formed in the single-crystalline silicon layer using the front-end doping and contact steps present for transistor fabrication. Ring resonators, shown in inset to Fig. 7(a), formed using the plasma-modulating rib waveguides function as amplitude modulators by tuning the resonance on and off resonance relative to the incoming laser frequency [31]. Since the optical mode is confined sufficiently

#163082 - $15.00 USD Received 15 Feb 2012; revised 29 Mar 2012; accepted 2 Apr 2012; published 15 May 2012
(C) 2012 OSA

far away from the optically-lossy contacts, the resonators' FWHM optical bandwidths were measured to be 60 GHz near 1260 nm and 45 GHz near 1550 nm as shown in Fig. 7(a). Accurate fabrication enabled close to critical-coupling of the modulators with 9 dB and 10 dB on-resonance extinctions near 1260 nm and 1550 nm respectively.

Low series resistance enables significant carrier injection at scaled-CMOS compatible voltages as shown in the inset of Fig. 7(e). Relying on carrier injection limits the modulation rates by the time constants for diffusion and recombination within the diode. The small signal bandwidth of the modulator was measured in a copy of the circuit-connected device that was accessible with 100 µm pitch ground-signal-ground pads. An Anritsu M3692B microwave synthesizer was input through a Picosecond Pulse Labs 5542 bias tee with 0.9 V forward bias and a 50 Ohm terminated (Midwest Microwave TRM-2106-MF-SMA-02) ground-signal-ground probe (Cascade Microtech i40-GSG-100). The resulting modulated power in the optical output was measured on a HP 70900B microwave spectrum analyzer with an internal optical frontend (HP 70810B). For the fabricated modulators, the measured small-signal bandwidth is below 1 GHz as shown in Fig. 6(e), consistent with carrier-injection modulators in non-integrated processes [31].

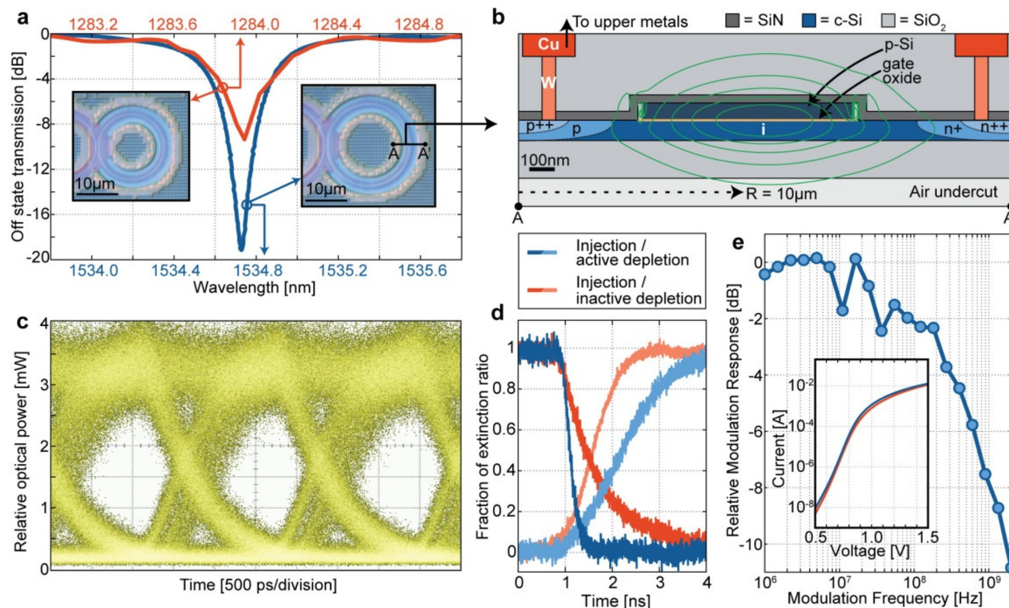

Fig. 7. Resonant electro-optic modulators were demonstrated using rib waveguide, carrier-injection phase shifters. (a) The optical transmission spectra with inset micrographs are shown for the 1280 nm (Q = 3970) and 1550 nm (Q = 4290) wavelength bands. The silicon slab layers are continuous in the coupling regions and 132 nm gaps and 122 nm gaps are formed between the polysilicon strips for the 1280 nm and 1550nm designs respectively. Cross-section cartoon of the 1550 nm device is shown in (b) to illustrate the lateral optical mode confinement, contours, and electrical contact regions. The eye diagram (c) demonstrates 600 Mbps data transmission with 10 dB on-off extinction ratio for the 1550 nm modulator integrated with a modulator driver. The step function time constant dependence on driver configuration (d) demonstrates the acceleration of carrier depletion under reverse bias, but at the expense of the carrier-injection time constant in the current integrated driver configuration for a 1280 nm modulator. The measured small-signal modulation electro-optic transfer response for a 1550 nm modulator is shown in (e) with the injection current as a function of diode bias voltage shown in inset for both modulators (1550 nm device in blue, 1280 nm in red).

Next, the integrated modulator driver was used to transmit data generated by the on-chip pseudo-random bit sequence (PRBS) generator shown schematically in Fig. 1. The generated eye diagram, shown in Fig. 7(c), demonstrates 10 dB on-off extinction in the resulting data

#163082 - $15.00 USD Received 15 Feb 2012; revised 29 Mar 2012; accepted 2 Apr 2012; published 15 May 2012
(C) 2012 OSA

stream. The integrated driver was designed as a configurable, all-digital, split-supply push-pull circuit with the schematic shown in Fig. 8. The integrated driver therefore allows for the electrical drive waveform to be switched from a zero-bias *off*-state, dominated by recombination, to a reverse-bias *off*-state, aided by drift-dominated carrier sweep-out, resulting in the output optical waveforms shown in Fig. 7(d). The optical eye diagram and step response were measured at 1550 nm on an Agilent 81600D sampling oscilloscope with a 30 GHz input bandwidth optical interface. The out-coupled signal from the chip was first amplified using an erbium doped fiber amplifier with the amplified spontaneous emission filtered using a band-pass filter. Due to the injection time constant and limitations of a single-polarity sub-bit pre-emphasis implemented in this chip, the achieved modulation rate in both wavelength bands is limited to 600 Mb/s achieved with a zero-bias off-state drive waveform. Further biasing and drive waveform optimization may raise the data rate well above 1 Gb/s for similar injection-based modulators by strong injection pre-emphasis [32]. Alternatively, the inherent speed limitation of carrier-injection-based designs may be overcome while improving energy efficiency by modulating the depletion-region width of a pn-junction formed with intermediate doping levels available in the process [33, 34].

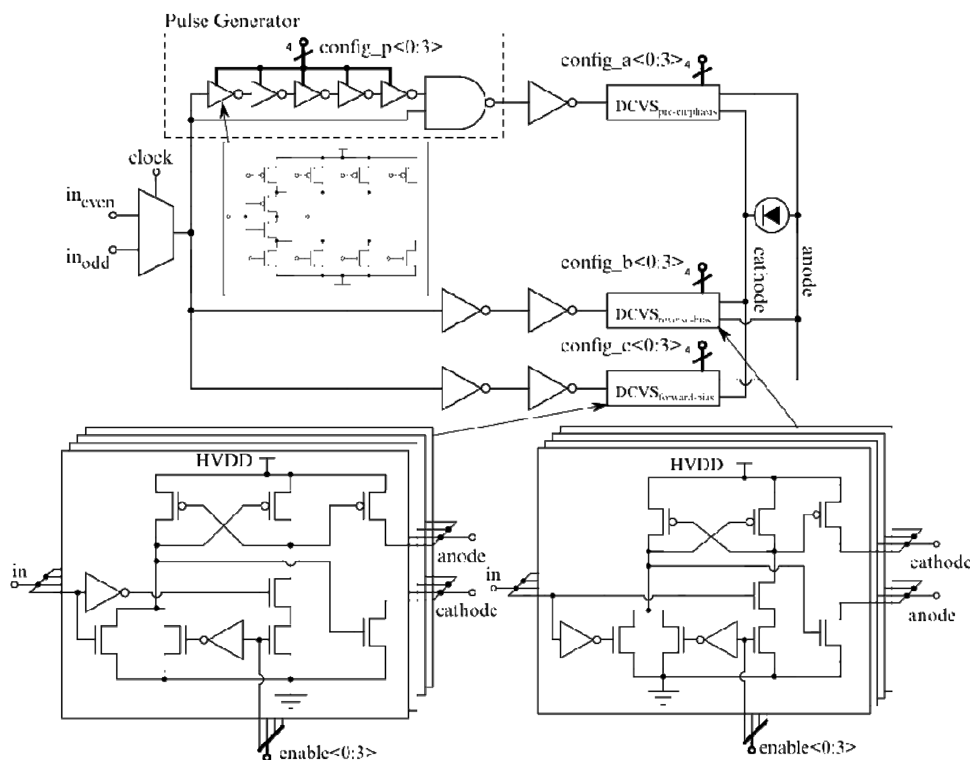

Fig. 8. Configurable, all-digital modulator driver circuit with split supplies and sub-bit pre-emphasis. The final driver stage utilizes split-supply to decouple increased modulator supply voltage from backend digital circuit supply to maintain backend circuit performance for various modulator supply conditions. Configurable forward and reverse bias drive strengths support a variety of modulator device designs on this platform.

7. Conclusions

The electronic-photonic platform demonstrated in this work is an accessible, low-cost utilization of the existing electronics foundry infrastructure to fabricate high-performance photonic devices alongside state-of-the-art CMOS transistors. Good passive photonic performance achievable with no in-foundry changes and simple post-processing using the

#163082 - $15.00 USD Received 15 Feb 2012; revised 29 Mar 2012; accepted 2 Apr 2012; published 15 May 2012
(C) 2012 OSA

thin-SOI-CMOS process removes the waveguide loss bottleneck present in previous work [9]. Devices such as the filter bank demultiplexer and modulator presented in this work, together with integrated photodetectors that are currently under development, form the basis of a photonic interconnect platform in an advanced electronics process that is used to fabricate microprocessors today [15]. The general-purpose nature of this foundry platform provides access to state-of-the-art technology that will greatly empower research into novel electro-optic systems-on-chip across the entire spectrum of VLSI and photonic systems and applications.

Acknowledgments

This work was funded by DARPA award W911NF-10-1-0412, and also in part by the NSF, the FCRP IFC, MIT CICS, and the Trusted Foundry. The views expressed are those of the authors and do not reflect the official policy or position of the Department of Defense or the U.S. Government.